

Dose, exposure time and resolution in serial X-ray crystallography

D. Starodub,^{a*} P. Rez,^a G. Hembree,^a M. Howells,^b D. Shapiro,^b H. N. Chapman,^c P. Fromme,^d K. Schmidt,^a U. Weierstall,^a R. B. Doak^a and J. C. H. Spence^a

^aDepartment of Physics, Arizona State University, PO Box 871504, Tempe, AZ 85287-1504, USA,

^bAdvanced Light Source, Lawrence Berkeley National Laboratory, Berkeley, CA 94720, USA,

^cLawrence Livermore National Laboratory, 7000 East Avenue, Livermore, CA 94550, USA, and

^dDepartment of Chemistry and Biochemistry, Arizona State University, PO Box 871604, Tempe, AZ 85287-1604, USA. E-mail: dmitri.starodub@asu.edu

The resolution of X-ray diffraction microscopy is limited by the maximum dose that can be delivered prior to sample damage. In the proposed serial crystallography method, the damage problem is addressed by distributing the total dose over many identical hydrated macromolecules running continuously in a single-file train across a continuous X-ray beam, and resolution is then limited only by the available molecular and X-ray fluxes and molecular alignment. Orientation of the diffracting molecules is achieved by laser alignment. The incident X-ray fluence (energy/area) is evaluated that is required to obtain a given resolution from (i) an analytical model, giving the count rate at the maximum scattering angle for a model protein, (ii) explicit simulation of diffraction patterns for a GroEL–GroES protein complex, and (iii) the spatial frequency cut-off of the transfer function following iterative solution of the phase problem, and reconstruction of an electron density map in the projection approximation. These calculations include counting shot noise and multiple starts of the phasing algorithm. The results indicate counting time and the number of proteins needed within the beam at any instant for a given resolution and X-ray flux. An inverse fourth-power dependence of exposure time on resolution is confirmed, with important implications for all coherent X-ray imaging. It is found that multiple single-file protein beams will be needed for sub-nanometer resolution on current third-generation synchrotrons, but not on fourth-generation designs, where reconstruction of secondary protein structure at a resolution of 7 Å should be possible with relatively short exposures.

1. Introduction

In order to solve the structure of proteins which are difficult to crystallize, we have proposed spraying them across a synchrotron X-ray beam and aligning them using the dipole moment induced by a near-infrared polarized laser (Spence & Doak, 2004; Starodub *et al.*, 2005). All three orthogonal intersecting beams (the single-file protein beam, the alignment laser and the X-ray beam) operate quasi-continuously (without synchronization) until an adequate signal-to-noise ratio is achieved in the diffraction pattern, which is then read out. By rotating the polarization of an elliptically polarized laser, this process may then be repeated for many orientations to fill the three-dimensional volume in reciprocal space with diffraction data. Other alignment methods, such as static electric or magnetic fields, or flow alignment have been

considered and demonstrated (Bras *et al.*, 1998; Koch *et al.*, 1988), as well as employed in the field of birefringence measurements (Fredericq & Houssier, 1973). These alignment techniques may also be helpful to avoid the problem of orientation classification of diffraction patterns from single molecules in random orientations, which is the main difficulty arising for single molecule imaging using pulsed X-ray free-electron lasers (Chapman *et al.*, 2006a; Huld *et al.*, 2003). The motion of the molecules does not affect the diffraction pattern if the illuminating wavefield is approximately planar, so that if there is, for example, one molecule in the beam at any instant, the method is equivalent to diffraction from a single stationary molecule. The continuous replacement of this molecule by others, however, allows an arbitrarily long exposure time without radiation damage. For 20 µm-diameter X-ray and laser beams, with a typical droplet beam velocity $v = 50 \text{ m s}^{-1}$,

the transit time through the beam is $t = 400$ ns. The radiation dose received by each protein during this time can be estimated by applying Bragg's rule of weighted summation of monatomic photoabsorption cross sections for the elements composing a protein. Using tabulated data on photoabsorption cross sections (Henke *et al.*, 1993), for a generic protein stoichiometry $\text{H}_{50}\text{C}_{30}\text{N}_9\text{O}_{10}\text{S}_1$ and density 1.35 g cm^{-3} , that gives a mass absorption coefficient μ of $9.6 \text{ cm}^2 \text{ g}^{-1}$ at an X-ray energy $E = 8 \text{ keV}$, required a near-atomic resolution to be obtained. The dose which sets the radiation damage limit at atomic resolution is $D_L = 2 \times 10^7 \text{ Gy}$ (Henderson, 1995). That assumes that an ejected photoelectron passes through surrounding bulk material causing damage, and therefore gives a lower limit on acceptable dose for the isolated biomolecules in serial crystallography, where the photoelectrons deposit only a small fraction of their energy before escaping into vacuum. Thus to damage the protein on the atomic scale during its transit time one would need a flux for 8 keV X-rays of $I_0 = D_L/\mu Et = 4.1 \times 10^{10} \text{ photons s}^{-1} \text{ nm}^{-2}$. Although at a lower X-ray energy the absorption coefficient increases, the radiation damage dose at the increased scale of resolution, feasible at this energy, increases as well. Therefore the maximum tolerable flux does not increase dramatically as X-ray energy decreases. This beam flux is far beyond the capabilities of any existing or projected X-ray sources. Therefore the resolution achievable in serial crystallography is not limited by radiation damage, and depends chiefly on the effectiveness of the alignment process (Spence *et al.*, 2005) and the time available for data collection.

If there is no interference between X-rays scattered from different molecules then the scattered intensity from a single-file train of macromolecules with separation L traveling across an X-ray beam of diameter $D_B = 20 \text{ }\mu\text{m}$ is proportional to the number of molecules falling within the beam at any instant, $M = D_B/L$. We further assume that all M molecules are perfectly aligned. For a monodispersed Rayleigh droplet beam, the droplet diameter is about twice that of the column of liquid from which they form by a necking instability (Rayleigh, 1878), and the spacing between droplet centers is about twice their diameter. Therefore, the $1 \text{ }\mu\text{m}$ liquid column produced by a Rayleigh droplet source gives $L = 4 \text{ }\mu\text{m}$ and $M = 5$, resulting in an 80% reduction in exposure time over single molecule exposure at the same resolution. In order to increase the scattering intensity, the design of 'shower head' aerodynamically formed multiple-jet nozzles is also under active development (Weierstall *et al.*, 2007). Experiments are planned with an average of one protein per droplet, and also with many proteins per droplet. Data will also be collected using an average of one sub-micrometer protein crystallite in each droplet. Even without alignment, the resulting 'powder protein data' might be solved by molecular replacement methods using the iterative flipping algorithm (Wu *et al.*, 2006). In this paper we treat mainly the case of one molecule per droplet, and assume that all water except a few-monolayer jacket of vitreous ice has been removed, as in recent research on proteins using electrospray spectroscopy (Sobott *et al.*, 2005), so that the ice-jacket effects can be ignored. Inclusion

of the ice background may increase the required dose by almost one order of magnitude; however, by choice of flight distance the jacket thickness may be reduced to zero.

The purpose of this paper is to provide a realistic estimation of the exposure time required for diffractive imaging of biological macromolecules. We perform simulations of the diffraction patterns for a sample object at various exposure times, and then apply the iterative procedure to solve the phase problem for charge density reconstruction in order to determine the relationship between exposure time Δt and resolution d in the reconstructed image. The results are compared with power-law estimates derived from simple scattering models.

Our project grew out of earlier work on coherent diffractive imaging (Marchesini, Chapman *et al.*, 2003) based on a soft X-ray undulator beam [beamline 9.0.1 at the Advanced Light Source (ALS)], using a zone plate as a monochromator. Diffraction from virus particles was intended, requiring 500 nm spatial coherence and high flux, made possible only by an undulator operating in the soft X-ray region. For large proteins or macromolecular assemblies at 20 Å resolution, shorter wavelengths and less coherence are needed, so that our simulations here are given for the new COSMIC beamline at the ALS with an undulator optimized for producing soft X-rays in the energy range 0.25–3 keV, for a new coherent 2–6 keV undulator beamline at the Advanced Photon Source (APS) and for the energy-recovery linac (ERL) source planned at Cornell.

2. Relationship between resolution and exposure time

Related treatments of the relationship between exposure, dose, resolution and beam energy for X-ray microscopy have been given previously (Howells *et al.*, 2005; Marchesini, Chapman *et al.*, 2003; Shen *et al.*, 2004). That work was based on calculation of the imaging dose (energy absorbed per unit mass) required to collect statistically significant data at a given resolution. If this dose is smaller than that known to destroy structural detail of a given size, this resolution is considered feasible. Otherwise, the resolution limit is determined by the dose that destroys detail of a given size. A statistically reliable photon count P , required for resolution d , may be found in either of two ways. The first approach is to calculate the total number of photons scattered into the detector from a single sample voxel with dimensions $d/2 \times d/2 \times d/2$. (These counts will subsequently be phased and recombined computationally into one resolution voxel in the real-space reconstruction or image.) Alternatively, one may calculate the number of photons scattered by the entire object of size D into one detector pixel at a scattering angle corresponding to the resolution of interest. The first method is independent of sample size, the second is not. Both methods depend on the structure of the object (in the first method the result depends on which voxel is chosen), so that resolution is here a property of the sample as well as the instrument. In the first approach (Howells *et al.*, 2005) one can simply integrate the signal,

scattered by a spherical voxel of diameter $d/2$, to obtain (Henke & DuMond, 1955)

$$P = (\pi/128)r_e^2\lambda^2d^4|\rho|^2I_0\Delta t \quad (1)$$

in the limit $\lambda \ll d$, where $r_e = 2.82 \times 10^{-6}$ nm is the classical radius of an electron, $\rho = \sum_i n_{ai}(f_{1i} + if_{2i})$ is the effective complex electron density of matter with multiple atomic concentrations n_{ai} and complex atomic scattering amplitudes $f_{1i} + if_{2i}$ for the i th type of atom, λ is the X-ray wavelength, I_0 is the incident X-ray flux and Δt is the data acquisition time. Then the dose, proportional to the incident X-ray beam fluence, scales with resolution as d^{-4} . The required exposure does not depend on detector size. In the second approach an incoherent sum over the object volume of the scattered intensities from the resolution elements (voxels) of size d into a detector pixel corresponding to resolution d is (Shen *et al.*, 2004)

$$P = (3/4\pi^3)r_e^2\lambda^2d^3D|\rho|^2I_0\Delta t. \quad (2)$$

This result depends on the object size and the shape of the resolution element. Note that if the latter were cubic, the scattered intensity at scattering vector $q = 2\pi/d$ corresponding to the resolution limit would be zero.

The generally accepted requirement for a statistically reliable measurement of signal P is that the signal exceeds the background noise level by a factor of five (Rose, 1948). This leads to the requirement for a minimum of $P = 25$ photons pixel $^{-1}$ for a recognizable image. But since the input to the numerical phase-retrieval algorithms involves the modulus of the scattered amplitude rather than intensity, for Poisson noise this implies $\sqrt{P}/(\Delta\sqrt{P}) = 2P/\Delta P = 2\sqrt{P} = 5$, or $P = 6.25$. Successful three-dimensional reconstruction from experimental diffraction patterns has been reported at a photon count of just 1 photon pixel $^{-1}$ at the highest achieved resolution (Chapman *et al.*, 2006b). To be consistent with previous work (Shen *et al.*, 2004), we therefore choose $P = 5$ for further discussion.

Because the coherence patch of the synchrotron is larger than our biomolecule, we assume that the statistical accuracy of a diffraction pattern is defined by the coherent scattering from the entire object at the angle that corresponds to the required resolution. For convenience we start by considering the scattering from a single organic spherical object of radius $R = D/2$. The incident X-ray wavevector is \mathbf{k} , the scattered wavevector \mathbf{k}' and the scattering vector \mathbf{q} . The vector \mathbf{q} connects the (000) point with other points on the momentum- and energy-conserving Ewald sphere of radius k ,

$$\mathbf{q} = \mathbf{k}' - \mathbf{k},$$

with the maximum value q_{\max} defined by the maximum scattering angle allowed by the detector geometry. To obtain a full three-dimensional reconstruction, diffraction patterns from all object orientations must be recorded, in order to fill a sphere of radius q_{\max} in reciprocal space. These intensities measured on the Ewald sphere can then be redistributed onto a regular Cartesian grid by interpolation. As our object is coherently illuminated by X-rays, with incident electric field E_0 , the

electric field amplitude at a distance r in a direction specified by \mathbf{q} is

$$E'(\mathbf{q}) = (r_e/r)E_0 \sin \psi \int \rho(\mathbf{r}) \exp(i\mathbf{q}\cdot\mathbf{r}) \, d\mathbf{r}, \quad (3)$$

where $\rho(\mathbf{r})$ is the charge density and ψ represents the angle between the electric field and the scattered direction (a polarization term). If the sphere had uniform charge density ρ , then the Fourier transform in (3) could be evaluated as

$$A(q) = 4\pi\rho R^3 \frac{\sin(qR) - (qR)\cos(qR)}{(qR)^3}. \quad (4)$$

In terms of a differential cross section $d\sigma_q/d\Omega$ the scattering intensity can be written as

$$I(q) = \frac{d\sigma_q}{d\Omega} \Delta\Omega I_0 = r_e^2 |A(q)|^2 \sin^2 \psi \Delta\Omega I_0. \quad (5)$$

To solve the phase problem using the scattered intensity pattern based on the iterative Fienup (1982) algorithm, the object must be embedded in a known matrix of extent sD , with sampling ratio $s = 2^{1/3}$ for three-dimensional reconstruction and $s = 2^{1/2}$ for two-dimensional reconstruction. Then the pixel size in reciprocal space is $\Delta q = \pi/sR$. If we consider scattering by relatively small angles, then the solid angle subtended by a pixel is

$$\Delta\Omega = \left(\frac{\Delta q}{k}\right)^2 = \left(\frac{\lambda}{2sR}\right)^2. \quad (6)$$

As seen from (4), the shape function for a uniform charge density falls as q^3 . Additionally, the atomic scattering factor also decreases for a larger scattering vector. This means that reconstructing an object to a given resolution d requires that there be statistically significant counts in a pixel at $q_{\max} = 2\pi/d$. If the detector has $N \times N$ pixels and its center is on the axis of the incident beam, then at the edge of the detector $q_{\max} = N\Delta q/2$. Then the expression for resolution becomes

$$d = 4sR/N. \quad (7)$$

From (4)–(6) we obtain for the scattered photon count P at the pixel corresponding to the scattering vector q ,

$$P = I(q)\Delta t = \frac{4\pi^2 r_e^2 \lambda^2 |\rho|^2 I_0 \Delta t}{s^2 R^2} \left[\frac{\sin(qR) - (qR)\cos(qR)}{q^3} \right]^2. \quad (8)$$

The oscillation period of the term in square brackets slightly exceeds the pixel size, and becomes equal to that at $s = 1$. Averaging of this term in a radial direction over the pixel size gives for small s

$$\frac{sR}{\pi} \int_{q-\pi/2Rs}^{q+\pi/2Rs} \left[\frac{\sin(qR) - (qR)\cos(qR)}{q^3} \right]^2 dq \simeq \frac{1}{2} \frac{R^2}{q^4}. \quad (9)$$

Combining (8) and (9) we obtain for the number of counts in time Δt at the pixel corresponding to resolution d ,

$$P = \frac{1}{8\pi^2 s^2} r_e^2 \lambda^2 d^4 |\rho|^2 I_0 \Delta t. \quad (10)$$

This expression has the same functional dependence as that obtained by Howells *et al.* (2005) but with a different numerical prefactor. We note in particular the power-law scaling with d and λ . A similar result is obtained in the phase-grating approximation, applied to one voxel. Here the phase shift $\varphi = r_c \rho \lambda d$, which produces a cross section $d^2 \varphi^2$, as above. It is also noteworthy that the cross section, which is proportional to $r_c^2 \lambda^2 d^4 |\rho|^2$, has now acquired a wavelength dependence. This may be somewhat unexpected since the total (Thomson) cross section is well known to be wavelength independent. The reason is that equation (10) and similar expressions have arisen by effectively integrating the differential cross section over a solid angular range (the detector acceptance) that is determined by the resolution choice and therefore does depend on the wavelength. This wavelength factor is also present in the Born approximation and the phase-grating approximation.

3. Scattering simulation

A more detailed analysis, extending to the important sub-nanometer resolution range, is possible using a direct calculation of the X-ray diffraction pattern based on atomic X-ray scattering factors. This allows the effects to be considered of three-dimensional atomic structure, detector size, noise and stability of our iterative algorithm for solution of the phase problem. As the test object for our simulations we choose the asymmetric *E. coli* chaperonin GroEL₁₄-GroES₇-(ADP-AIF_x)₇ protein complex, constituted of 59276 non-hydrogen atoms. GroEL contains 14 identical subunits of molecular mass 58 kDa, and GroES contains seven subunits of molecular mass 10 kDa. They form a structure consisting of three distinctive rings. The length of the complex is 20 nm, with diameter 14.5 nm. The three-dimensional structure of the complex at 2.8 Å resolution has been reconstructed by X-ray crystallography (Chaudhry *et al.*, 2004) and was obtained from the Protein Data Bank (entry 1SVT). A sketch of the scattering geometry is shown in Fig. 1. The detector is a two-

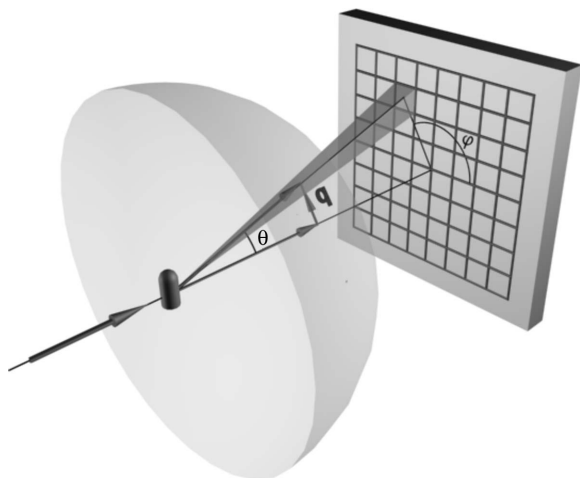


Figure 1
Scattering geometry for simulation of diffraction pattern.

dimensional 512×512 array of equidistant pixels of linear size a , located at a distance l_{00} from the sample, which limits the scattering angle at its edges to a resolution of a few angstroms. The position of a pixel with indices i and j relative to the sample is defined by the zenith angle θ_{ij} (which also determines the distance l_{ij} between this pixel and the sample) and azimuth angle φ_{ij} . Then the diffraction pattern is formed by the polar gnomonic projection of the points lying on the Ewald sphere onto the flat detector screen. According to (5), for an incident plane wave of intensity I_0 with wavelength λ the scattered photon count per unit time in the given pixel is given in the single-scattering (Born) approximation as

$$I_{ij} = r_c^2 A(q_{ij}) A^*(q_{ij}) \sin^2(\psi_{ij}) \Delta\Omega_{ij} I_0, \quad (11)$$

with a sample scattering amplitude

$$A(q_{ij}) = \sum_k f_k(q_{ij}) \exp(i \mathbf{q}_{ij} \cdot \mathbf{r}_k), \quad (12)$$

where $q_{ij} = 4\pi \sin(\theta_{ij}/2)/\lambda$ is the scattering vector corresponding to detector pixel (i, j) , which subtends solid angle $\Delta\Omega_{ij} = a^2 \cos(\theta_{ij})/l_{ij}^2$ at the angle θ_{ij} . \mathbf{r}_k is the position vector of the k th atom in the sample, and the summation is performed over all the atoms of the sample. For the undulator odd harmonics the X-ray beam is linearly polarized and the polarization term is

$$\sin^2(\psi_{ij}) = 1 - \sin^2(\theta_{ij}) \cos^2(\varphi_{ij}).$$

The scattering amplitude for the k th atom is (Henke *et al.*, 1993)

$$f_k(q) = f'_k + i f''_k - \Delta f_k(q),$$

where the last term describes the angular dependence of the atomic form factor,

$$\Delta f_k(q) = Z - \tilde{f}_k(q),$$

and $\tilde{f}_k(q)$ is the empirical approximation of tabulated data by four-Gaussian fitting (Doyle & Turner, 1968), satisfying the condition $\tilde{f}_k(0) = Z$. We note that if absorption is neglected so that $f_k(q)$ is real, then $A(-\mathbf{q}) = A^*(\mathbf{q})$, and the charge density obtained by Fourier transform of the sample scattering amplitude is real.

To satisfy the Shannon sampling requirement, the maximum allowed beam angular spread at the sample should be equal to $\theta_c = \lambda/2sD$ (Spence *et al.*, 2004). For $s = 2^{1/2}$, $D = 200$ Å and the X-ray energies of 3, 5.4 and 8 keV used below, the angular spreads that can be accepted are 7.3, 4.1 and 2.7 mrad, respectively. The requirement that wavetrains from opposite sides of the sample interfering at the edge of the detector should have at least 50% overlap leads to a condition on the coherence length of the illuminating beam which can be expressed as $\Delta\lambda/\lambda < 2/N$ (Chapman *et al.*, 2006b; Spence *et al.*, 2004), where N is the number of pixels along one Cartesian axis. According to (7) with a sampling ratio $s = 2^{1/2}$, and $D = 200$ Å, a resolution of 7 Å requires 81 pixels. Then the desired energy bandwidth is 2.5%. The above values for the beam angular spread and the size of the interaction region ($20 \mu\text{m} \times 20 \mu\text{m}$) define the volume of the beam transverse phase space

that can be accepted by the scattering experiment. Since the undulator cannot fill this phase space (nor the 2.5% bandwidth), we assume that all phase space of the actual X-ray beam can be used. This situation is typical of a ‘flux experiment’ in synchrotron parlance.

We perform simulations of the diffraction patterns from the GroEL–GroES protein complex using the parameters of three new X-ray beamlines that will become available in the near future. The first one is the recently proposed COSMIC beamline at section 7 of the ALS, which will provide brightness B larger than 10^7 photons $s^{-1} \text{ nm}^{-2} \text{ mrad}^{-2}$ (0.1% bandwidth) $^{-1}$ in the energy range 0.25–3 keV. It will be advantageous for flux to operate at the minimum possible energy that is capable of (a) penetrating the sample and (b) achieving the desired resolution at a reasonable Bragg angle. On this basis the best choice for the case at hand is 3.0 keV. The width and angular spread of the X-ray beam are determined by a convolution of the one-electron undulator pattern with the spread functions of the electron beam in width and angle (Spence & Howells, 2002). Using parameters for the COSMIC undulator at 3 keV, we find the X-ray root mean square (r.m.s.) horizontal width $\sigma_{Tx} = 0.293$ mm and vertical width $\sigma_{Ty} = 8.53$ μm , r.m.s. angular spread $\sigma_{Tx'} = 25.9$ μrad and $\sigma_{Ty'} = 14.9$ μrad in the horizontal and vertical directions, respectively. Then the X-ray intensity at the sample is $I_0 = (2\pi)^2 B \sigma_{Tx} \sigma_{Ty} \sigma_{Tx'} \sigma_{Ty'} / A = 0.95 \times 10^6$ photons $s^{-1} \text{ nm}^{-2}$ at 0.1% energy bandwidth. Taking into account the estimated 76% loss in the presumed optical system (multilayer monochromator and focusing system) and adjusting for the maximum bandwidth $\Delta\lambda/\lambda = 1/151$ possible at 3 keV, we finally obtain $I_0 = 1.5 \times 10^6$ photons $s^{-1} \text{ nm}^{-2}$. Since the phase-space volume in one dimension of a single mode beam is $\lambda/4\pi$, the total number of modes in the beam is $231 \times 3.87 = 894$.

The second example considers the projected undulator source at APS, which will operate in the energy range between 2 and 6 keV. A recent measurement of the similar undulator beam at sector 7 of the APS, focused into a 10 μm spot, gave 6×10^{12} incident photons s^{-1} with a beam divergence of 1.4 mrad at 0.01% energy bandwidth at 14.3 keV (Young *et al.*, 2006). The same analysis as for the COSMIC beamline gives an optimized beam intensity of 1.8×10^6 photons $s^{-1} \text{ nm}^{-2}$ at 5.4 keV. For the harder X-rays, suitable for higher resolution, we use a flux of 3×10^8 photons $s^{-1} \text{ nm}^{-2}$ at 8 keV, corresponding to the proposed ERL beamline at Cornell University (Shen *et al.*, 2004).

The secondary structure of proteins (α -helices) can be resolved at a resolution of $d = 7$ \AA , which sets the lower limit for the largest measured scattering vector as 0.9 \AA^{-1} . The sampling ratio can be found from (7) as $s = Nd/2D$. Several definitions of ‘oversampling ratio’ have appeared in the literature; here we define oversampling as the ratio of the actual sampling ratio s to the minimum acceptable one. Then, for a two-dimensional projection, oversampling is $Nd/2^{3/2}D$. Thus, for a detector whose linear size is $N = 512$ pixels and $D = 200$ \AA the diffraction pattern is oversampled by a factor of 6.3, if the required resolution is 7 \AA . A simulated diffraction pattern, on the 512×512 grid for one molecule in the 8 keV

X-ray beam, is presented in Fig. 2(a), while Fig. 2(b) shows the scattered intensity per pixel, averaged over the azimuth angle, as a function of scattering vector for incident beam energies of 3.0, 5.4 and 8.0 keV with intensities of 1.5×10^6 , 1.8×10^6 and 3×10^8 photons $s^{-1} \text{ nm}^{-2}$, respectively. If normalized to the same incident flux, the ratio of the integrated scattered intensities (scattering cross sections) for 3.0, 5.4 and 8.0 keV is 7.3:2.2:1. This is close to the ratio 7.1:2.2:1 predicted by a λ^2 scaling of scattered coherent flux with X-ray wavelength, according to equation (1). Lower X-ray energy can require a

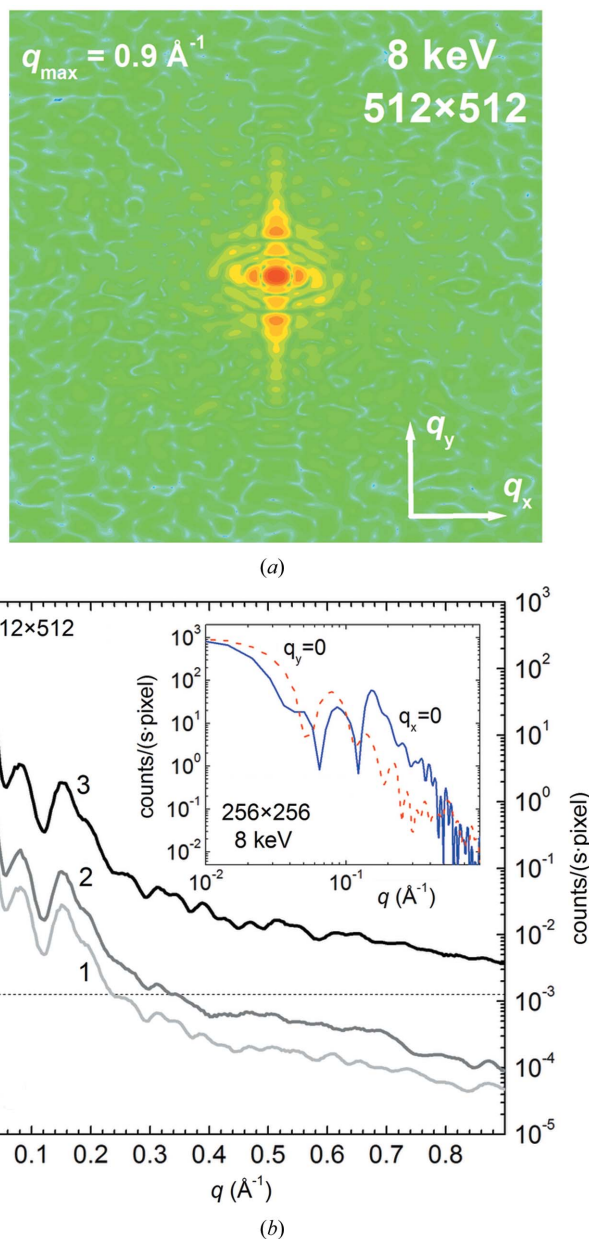


Figure 2
 (a) Diffraction pattern for the GroEL complex at an X-ray energy of 8 keV. (b) Scattered intensity per pixel after angular averaging at: (1) 5.4 keV and 1.8×10^6 photons $s^{-1} \text{ nm}^{-2}$ (APS); (2) 3.0 keV and 1.5×10^6 photons $s^{-1} \text{ nm}^{-2}$ (ALS); (3) 8.0 keV and 3×10^8 photons $s^{-1} \text{ nm}^{-2}$ (ERL). The inset shows the scattered counts per pixel for the incident flux (3) on the 256×256 grid, cut through the planes $q_x = 0$ (solid line) and $q_y = 0$ (dash line), indicated in (a). This figure will appear in colour in the online version of the paper.

closer distance between detector and sample in order to collect the data at large scattering angles. In this case the pixel size in reciprocal space near the center of the detector will be larger than the average, and failure to interpolate the diffraction pattern onto a regular grid of scattering wavevectors would result in a 'stretched' reconstructed object. Additionally at large scattering angles the count rate is affected owing to reduction of the solid angle subtended by a pixel near the edge of the detector by a factor of $\cos(\theta)$. The dotted horizontal line in Fig. 2(b) corresponds to five counts per pixel after exposure of 100 s at minimum required sampling ($N = 81$) for one sample in the X-ray beam at any instant. Therefore its intersections with the scattering curves at different X-ray energies determine the resolution achievable under these conditions. The sufficient statistics in a single two-dimensional projection from the three-dimensional tomographic data set, required for full reconstruction of the secondary protein structure, can be predicted in a 30 s exposure at the future ERL source, while the same result would require 1300 s at ALS and 2500 s at APS. For M proteins in the beam at any instant, the count rate is multiplied by M , since no interference occurs between different molecules. Therefore, with a reasonable assumption of $M = 15\text{--}30$, a resolution of 7 \AA in 100 s is feasible at the APS and ALS as well. Object reconstruction from these diffraction patterns (with noise added), as described in the next section, shows that larger exposure times than predicted here are actually required for the intended resolution. Note that full three-dimensional reconstruction requires that the collected data be assigned to points on the Ewald sphere, which is swept through reciprocal space (by rotating the sample) to fill a three-dimensional volume. Using diffraction patterns from different protein orientations independently would then increase tremendously the time required for data acquisition. However, if the correlation between various projections is taken into account for three-dimensional reconstruction according to the dose fractionation theorem (Hegerl & Hoppe, 1976), the dose required for each projection in the three-dimensional imaging will be reduced. The Hegerl–Hoppe theorem states that the full three-dimensional reconstruction of an object requires the same total dose (distributed over many orientations) as the reconstruction of a single two-dimensional projection at the same resolution. It is important to note that the scattering signal must be statistically reliable to resolve a single three-dimensional pixel in the two-dimensional projection, rather than a two-dimensional pixel formed by summation of three-dimensional pixels along the projector line (McEwen *et al.*, 1995). Thus the dose required for resolution d can be determined by considering scattering from an object slice of thickness $d/2$. The 3.5 \AA -thick slice of the GroEL contains about 1/40 of all atoms in the complex. Then the average count rate for that slice at the scattering angle corresponding to resolution d is 1/40 of that calculated above for the whole object. Correspondingly, the total dose required for the GroEL three-dimensional reconstruction is 40 times larger than the dose needed for the statistically accurate measurement of one orientation.

In the inset of Fig. 2(b) the scattering curves for 8 keV photons with an incident flux of $3 \times 10^8 \text{ photons s}^{-1} \text{ nm}^{-2}$ (ERL) in the planes of $q_x = 0$ (solid line) and $q_y = 0$ (dash line) are re-plotted using log–log coordinates. They are extracted from the 256×256 grid (sampling ratio $s = 4.48$). As expected for an asymmetric object, at smaller scattering vectors the scattering curves are feature-rich and highly inhomogeneous. In particular, a pronounced peak at $q_y = 0.15 \text{ \AA}^{-1}$ corresponds to the ring structure of the GroEL complex in the y direction with a period of about 40 \AA . It should be clear that in this scattering vector region it would be difficult to rely upon the general form of a power law (as derived in the previous section) for the required flux estimation, since the scattering curve in this region cannot be fitted by a power law. Owing to the sharp peak at 0.15 \AA^{-1} , this feature will dominate even in very noisy diffraction patterns, giving rise to a disc-like structure. The scattering curves become relatively featureless and independent of azimuth angle only at the highest scattering vectors, and then they can be approximated using a power law, resulting in the power scaling of the required exposure time with resolution, described in the previous section.

In the discussion above, we have defined resolution by the highest scattering angle at which statistically accurate data above background can be found in a detector pixel. This treatment does not take into account the stability of the reconstruction algorithm, used for phase retrieval, with respect to statistical fluctuations. Therefore, it gives a lower limit for the required exposure. In the next section we apply the hybrid input output (HIO) algorithm to reconstruct the high-resolution structure of the GroEL complex, and quantitatively investigate resolution as a function of incident fluence.

4. Coherent transfer function for HIO reconstruction

Because the HIO algorithm is known to be more effective for real-valued objects, where a strong positivity constraint can be applied, we limit our consideration to a real object. In the general case the Fourier transform of the scattering amplitude $A(\mathbf{q})$, collected on a two-dimensional grid, would not be real because one measurement cuts reciprocal space along the curved Ewald sphere, which does not contain points with inverted coordinates, and therefore the condition for object reality $A(-\mathbf{q}) = A^*(\mathbf{q})$, while satisfied by a tomographic data set collected in three dimensions, is not met on a two-dimensional grid. For simplicity, we do not consider such a full three-dimensional reconstruction, and to be consistent with the requirement of object reality we use the diffraction pattern from a two-dimensional projection of the GroEL–GroES electronic density, calculated by setting coordinate $z = 0$ in (12). This also avoids the de-focusing effects in the projection approximation for three-dimensional objects owing to the curvature of the Ewald sphere. We assume that the atomic scattering amplitude is equal to the number of electrons in atom Z , thus neglecting absorption and any angular dependence of scattering amplitude, which is justified for high-energy photons (here 8 keV) and scattering at small angles.

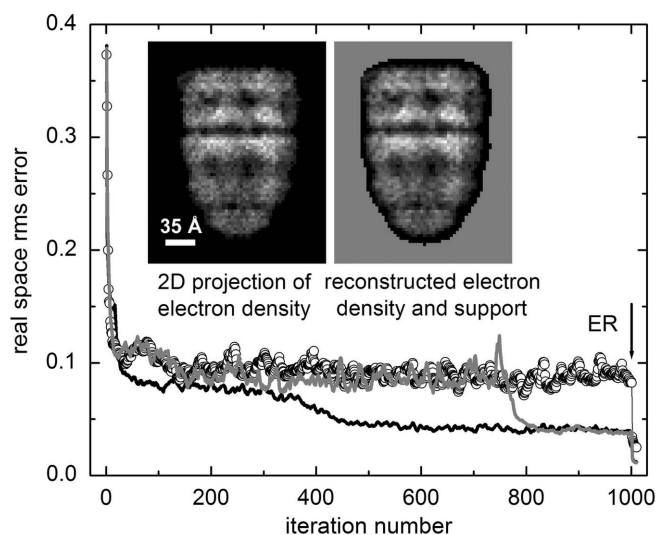


Figure 3 Real-space error for the HIO algorithm as a function of iteration cycle number. Solid lines show the error behavior for two successful runs, while circles correspond to the reconstruction, which did not converge to the solution. The arrow indicates the step where the error-reduction (ER) algorithm was applied. Inset: the charge density projection of the protein complex used to calculate the diffraction pattern (left panel) and averaged reconstruction (right panel). The area outside the support is filled with gray color. The bar length is 35 Å (ten pixels).

The projection of the object electronic density is given in the inset to Fig. 3 (left panel). The scaling bar length corresponds to 35 Å. The diffraction pattern was calculated on a 256×256 grid with a maximum wavevector transfer of $q_{\max} = 0.9 \text{ \AA}^{-1}$ (sampling ratio $s = 4.48$). We found that application of the HIO algorithm to a 128×128 grid ($s = 2.23$) decreases the percentage of successful reconstructions by a factor of 1.8.

The HIO iterative algorithm (Fienup, 1982) with reality and positivity constraints is described by a recursion relationship

$$g_{n+1}(\mathbf{r}) = \begin{cases} \hat{P}_M g_n(\mathbf{r}), & \text{if } \mathbf{r} \in S \wedge \Re[\hat{P}_M g_n(\mathbf{r})] \geq 0, \\ (1 - \beta \hat{P}_M)g_n(\mathbf{r}), & \text{otherwise,} \end{cases} \quad (13)$$

where $g_n(\mathbf{r})$ is the reconstructed object in real space after the n th iteration, S defines a support such that $g(\mathbf{r} \notin S) = 0$, \Re is the real part of the complex number, and the feedback parameter is $\beta = 0.9$. The projector operator \hat{P}_M determines the projection of the Fourier transform of the reconstructed object on the reciprocal space subset satisfying the modulus constrain defined by the measured scattered intensities,

$$\hat{P}_M g_n = F^{-1} \left\{ \frac{F(g_n)}{|F(g_n)|} [I(\mathbf{q})]^{1/2} \right\}. \quad (14)$$

Here $F(g_n)$ denotes the Fourier transform operation. We use 1000 cycles of the HIO iterations followed by five cycles of the error-reduction (ER) algorithm $g_{n+1}(\mathbf{r}) = \hat{P}_S \hat{P}_M g_n(\mathbf{r})$, where the support projector is

$$\hat{P}_S g_n(\mathbf{r}) = \begin{cases} g_n(\mathbf{r}), & \text{if } \mathbf{r} \in S \wedge \Re[g_n(\mathbf{r})] \geq 0, \\ 0, & \text{otherwise.} \end{cases} \quad (15)$$

The quantitative measure of the iterative process convergence is the error metric in real space (equal to the normalized amount of charge density remaining outside the support),

$$E_n^S = \left[\frac{\sum_{\mathbf{r} \notin S} |g_n(\mathbf{r})|^2}{\sum_{\mathbf{r} \in S} |g_n(\mathbf{r})|^2} \right]^{1/2}, \quad (16)$$

and, in reciprocal space,

$$E_n^M = \left\{ \frac{\sum_{\mathbf{q}} ||F(g_n)| - [I(\mathbf{q})]^{1/2}|^2}{\sum_{\mathbf{q}} I(\mathbf{q})} \right\}^{1/2}. \quad (17)$$

We determined the support by convolution of the known object, used for the calculation of the diffraction pattern, with a Gaussian whose half width at half-maximum was 3 pixels (10.5 Å), and a subsequent cut-off at 5% of the maximum object charge density. The area outside the support is marked by the gray color in the right-hand panel of the inset of Fig. 3. Because the support is relatively loose, the actual sampling ratio s (which should be more correctly defined relative to the support size rather than the object size, as we do here) is somewhat smaller than indicated. Even without using the support, the HIO algorithm provides the low-resolution sample structure and external boundary. This implies that the *Shrinkwrap* algorithm (Marchesini, He *et al.*, 2003) could be applied if the support were unknown. That algorithm dynamically refines an initially loose support using intermediate reconstructions after a series of iterative steps.

The first object estimation was determined by applying the support projector given by equation (15) to the Fourier transform of the measured modulus of the scattered amplitude $[I(\mathbf{q})]^{1/2}$ with random phases $\varphi(\mathbf{q})$. To ensure the reality of this Fourier transform, the condition $\varphi(-\mathbf{q}) = -\varphi(\mathbf{q})$ was enforced. In spite of the support asymmetry, sometimes the reconstructed image appeared in the inverse orientation. Although usually it rotates to the correct position after a sufficiently large number of iterations, in order to facilitate the convergence rate the first 100 iterations are performed additionally using the same set of random phases, but with reversed signs. Then the reconstructed object with the larger error, which has an incorrect orientation, is rejected, and the rest of the iterations are performed using the remaining object with the correct orientation.

Fig. 3 shows the behavior of the r.m.s. error, defined by (16), in a single reconstruction procedure for three reconstructions with different initial phases. In all cases, after a few iterations the error drops to $E^S \leq 0.1$. The successful reconstructions (solid lines, rate of success $\sim 85\%$) are characterized by a step-like decrease of the error by about a factor of two at some point (in Fig. 3, after around 400 and 800 iterations), which is accompanied by a decreasing of the error standard deviation. Reconstructions that do not converge to the correct solution have a persistently high and noisy error (open circles). Before averaging over successful reconstructions, the images must be re-positioned to accommodate for the origin ambiguity

produced by different random starting phases. This was done in two ways: by adjusting the image position in real space and the phases in reciprocal space. The reconstructed image with the smallest r.m.s. error was chosen as a reference. Then, in real space, each remaining image was translated to the position where its cross-correlation with the reference image has a maximum, in order to minimize the r.m.s. error between this and the reference images (Fienup, 1997). In reciprocal space, the linear shift of the reconstructed object is given by the slope of the difference map $\Delta\varphi(\mathbf{q})$ between the diffraction amplitude phases of this and the reference images. We compute the slopes $\Delta\varphi_x = \partial\Delta\varphi/\partial q_x$ and $\Delta\varphi_y = \partial\Delta\varphi/\partial q_y$ using the least-square linear fit in the q_x and q_y directions of the central part of the phase difference map, where the noise of the recovered phases has a lowest value. In most cases we define the central data segments for the linear fit by the condition that the correlation coefficient for these segments, reflecting their linearity, is set equal to 0.9. Then the image translation along the x axis in real space (in pixels) is determined as $X = \Delta\varphi_x N / 2\pi$, and similarly for the y direction. The image averaged over 171 successful reconstructions (out of 200), adjusted using the cross-correlation function, is shown in the right-hand inset of Fig. 3. It clearly repeats the original image structure. In particular, the details of the top *trans* GroEL ring, medium *cis* GroEL ring, and bottom GroES cap can be observed.

To test the stability of the HIO algorithm convergence with respect to the noise level, we introduced shot noise for the number of photons collected by a detector, described by a Poisson distribution of counts in each pixel,

$$p_{ij}(k) = \exp(-s_{ij})s_{ij}^k/k!,$$

where k is the integer number of counts in the (i, j) pixel, and $s_{ij} = I(q_{ij})M\Delta t$ is the expected number of counts in this pixel after exposure time Δt , determined from the calculated diffraction pattern. We assume an incident photon flux of 3×10^8 photons $\text{s}^{-1} \text{nm}^{-2}$ (ERL) and one sample in the beam at a time $M = 1$. Then the phase-retrieval algorithm was applied as described above. For each exposure time, 200 independent reconstructions have been run, and 15% of the reconstructions with the highest error have been rejected. The real-space r.m.s. error after the final iteration step, calculated according to equation (16) and averaged over successful reconstructions, is shown in Fig. 4(a) as a function of exposure time. The mean error steadily increases as the input diffraction patterns become noisier, roughly following the power dependence on the counting time with an exponent of -0.28 , as indicated by the fitting line. The images have been adjusted by either their positions or phases, as described above, and then averaged. The result is shown in Fig. 5 for both methods of image adjustment. Using the cross-correlation function in real space gives somewhat better images at low exposures. The details of the ring structure remain consistent at exposures as low as 10 s, but eventually they become completely smeared out at an exposure of 1 s, which is attributed to the fast growth of the HIO process instability at this counting time. The failure of the reconstruction algorithm is also reflected in the behavior of

the error distribution, shown in Fig. 4(b). In a large range of the longer exposure times, the errors of independent reconstructions have a very narrow and asymmetric distribution, which suddenly broadens as exposure decreases from 10 s to 1 s, indicating stagnation of the algorithm.

Visual examination of Fig. 5 allows one to follow the change of resolution in response to exposure time. Quantitative measure of resolution can be provided by the analysis of the transfer function (TF). If the Fourier transform of the reconstructed object $G(\mathbf{q})$ is considered as the output of the phase-retrieval algorithm, then its TF for diffraction amplitude modulus can be defined as the ratio of the modulus of the output averaged over independent reconstructions to the modulus of the ideal scattered amplitude (Shapiro *et al.*, 2005),

$$\text{TF}(q) = \frac{\langle |G(\mathbf{q})| \rangle_\varphi}{\langle [I(\mathbf{q})]^{1/2} \rangle_\varphi}. \quad (18a)$$

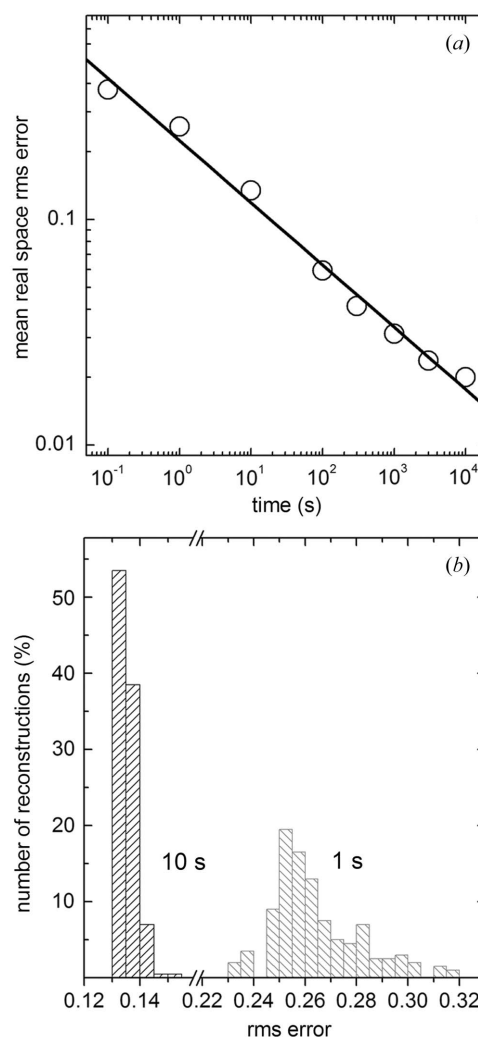


Figure 4
(a) Reconstruction r.m.s. error in real space, averaged over many independent reconstructions, as a function of counting time. The solid line shows the best fit to the data points by a power law. (b) Distribution of the r.m.s. error in two sets of independent reconstructions for counting times of 10 s and 1 s.

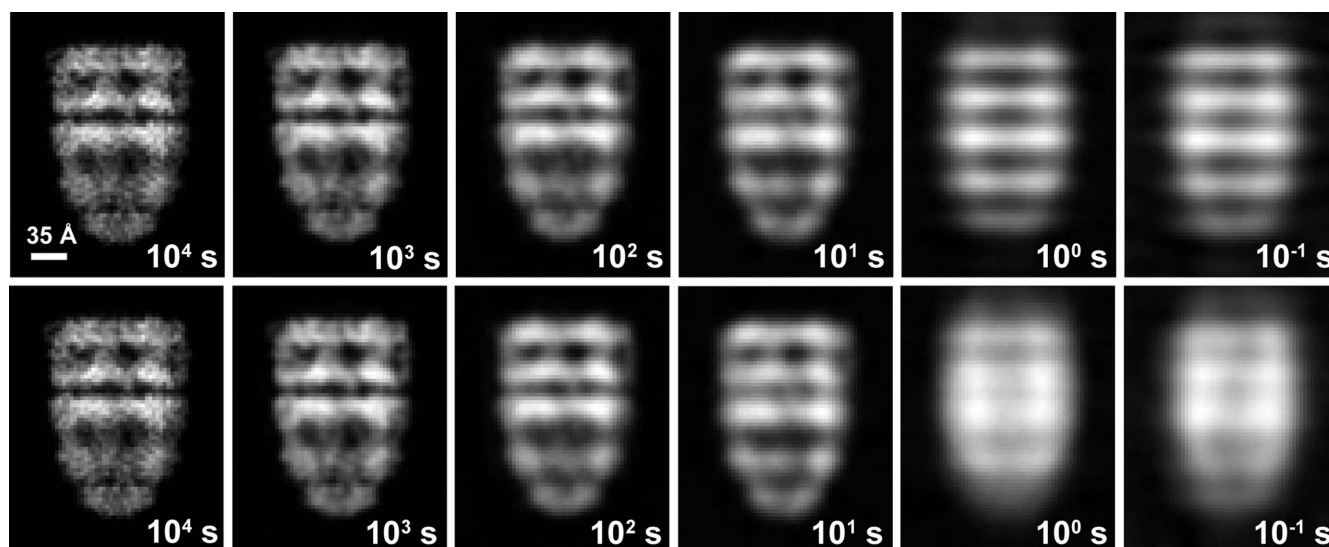


Figure 5
The series of averaged reconstructed charge density maps for the indicated exposure times. Before averaging, the images are positioned by translation in real space (top row) or by phase adjustment in reciprocal space (bottom row). The incident flux is 3×10^8 photons $s^{-1} nm^{-2}$ and the X-ray energy is 8 keV.

Here the Fourier transform moduli have been averaged over azimuth angle prior to the TF calculation. Averaging over reconstructions is denoted by $\langle \dots \rangle$, and $\langle \dots \rangle_\varphi$ corresponds to the averaging over azimuth angle. Alternatively, one can use the phase transfer function (Marchesini *et al.*, 2005), which does not require knowledge of the ideal scattering amplitude,

$$PTF(q) = \left\langle \left\langle \frac{G(\mathbf{q})}{|G(\mathbf{q})|} \right\rangle \right\rangle_\varphi. \quad (18b)$$

Then the resolution can be evaluated from the TF scattering wavevector cut-off. The plots of the TF, corresponding to different data acquisition times and therefore different signal-to-noise ratios, are shown in Fig. 6. The top row of images in Fig. 5 was used to obtain the curves in Fig. 6. Averaging of the reconstructed objects using phase information produces similar curves. The thick line (1) corresponds to the ideal diffraction intensity, being the input for the HIO procedure. It reflects the effects of imperfect phasing by the iterative algorithm itself, and exhibits a flat plateau at lower scattering vectors with a rather abrupt cut-off, characteristic of a coherent imaging system. Other curves demonstrate the TF response to the introduction of shot noise. We determined the resolution limit for a given exposure time from the width $q_{1/2}$ of the corresponding TF at half-maximum (TF = 0.5) as $d = 2\pi/q_{1/2}$. The results are shown in Fig. 7 in the form of a plot of data acquisition time as a function of resolution, for images averaged in reciprocal (solid squares) and real (open circles) space. Both sets of data points follow the power law at high resolution, but experience a sharp decrease at about 30 Å. This is especially obvious for the images averaged in real space, where apparent resolution becomes virtually independent of exposure. This effect is related to the specific features of the object structure, dominated by the well defined rings with average periodicity of 40 Å. Therefore, at lower exposure

time only the strong scattering due to these rings would be reliably detectable, even at very short counting times. In this case the phasing algorithm does not properly retrieve the phases of the scattering amplitude, as demonstrated in Fig. 5 by the blurring of the images averaged in reciprocal space. But it still produces the distinctive strips, which do not vanish upon real-space averaging. The overall object shape is recovered better when averaging is performed in reciprocal space. For the linear fit of the data we used only the five points giving the highest (best) resolution, where the required time obeys the power scaling with d . For the images averaged in reciprocal space, the exponent of the power law is -3.7 (-3.6 for the real-space averaging), in good agreement with equation (10).

For a quantitative comparison with the analytical results of §2, we assume an empirical protein composition of

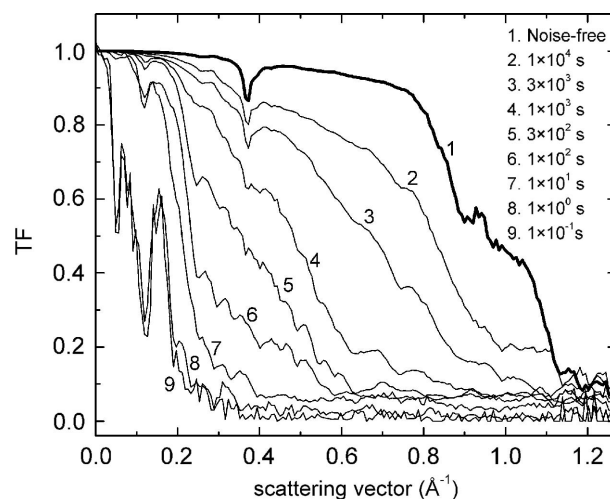


Figure 6
HIO transfer function for different signal-to-noise ratios (exposure times).

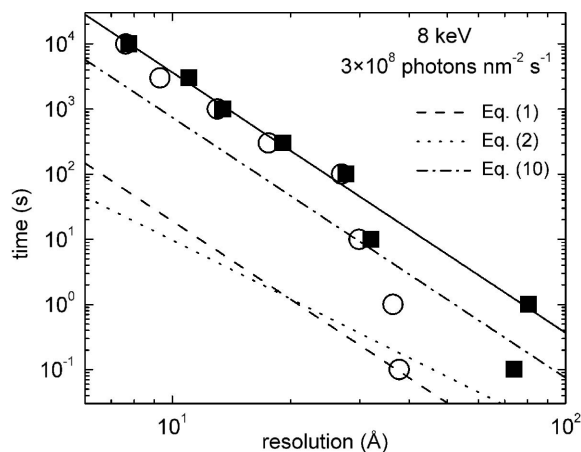


Figure 7 Exposure time requirement for a given resolution, deduced from the width of the TF for the HIO algorithm with output averaged using phase adjustment in reciprocal space (solid squares) and cross-correlation in real space (open circles). The solid line is the least-squares linear fit to the former data set for resolution higher than 30 Å. Other lines are given for comparison with simple analytical predictions from Howells *et al.* (2005) (dashed line), Shen *et al.* (2004) (dotted line) and this paper (dash-dotted line) with parameter $P = 5$.

$\text{H}_{50}\text{C}_{30}\text{N}_9\text{O}_{10}\text{S}_1$ and density 1.35 g cm^{-3} , which gives an average electron density of 434 nm^{-3} . We also take into account that equation (2) is derived for critical sampling, and rescale it to the sampling ratio of the 256×256 grid according to $\Delta t \propto s^2$. The resolution predicted by equation (10) at a given time (dash-dotted line) is better by a factor of 1.5 than that derived from simulated images. This discrepancy may be due partially to the additional effect of shot noise on the phasing algorithm stability, and to the arbitrarily setting of the number of counts required for the data statistical accuracy in the analytical solution, that appears to be too low. The possible reason is that the variation in scattered intensity rather than absolute count rate must be accurately measured, which would require a better signal-to-noise ratio. Considering the count rate P in the pixel at the resolution limit as a free parameter in our analytical model, the resolution, determined from the TF calculation and shown in the Fig. 7 by solid squares, can be exactly fitted by equation (10). However, the actual count rate, required for a given resolution, is higher than that expected from Fig. 2(b) and the Rose criterion. Fig. 7 also shows the required time dependencies on resolution described by equation (1) owing to Howells *et al.* (2005) (dashed line) and equation (2) by Shen *et al.* (2004) (dotted line). These curves give too optimistic results for the expected resolution as compared with the explicit TF calculation; however, we note that the fit would be improved by taking $P = 25$. The resolution definition *via* TF is still uncertain owing to its complicated shape and absence of a sharp cut-off, emphasizing that, for phase-contrast imaging, resolution cannot be specified by a single parameter, and depends on the sample itself. In Fig. 5 we observe that details of the shape envelope distort at counting times of less than 100 s. Collecting data at the critical sampling ratio would reduce the required exposure by a factor of 12.6. However, we found that

Table 1 Exposure time (s) required to achieve a given resolution at different X-ray beamlines with parameters, discussed in the text, calculated from equation (19) for $s = 2^{1/2}$ and $M = 10$.

| | $d = 0.7 \text{ nm}$ | $d = 1 \text{ nm}$ | $d = 2 \text{ nm}$ |
|-----|----------------------|--------------------|--------------------|
| ALS | 4.2×10^3 | 1.0×10^3 | 63 |
| APS | 1.1×10^4 | 2.7×10^3 | 171 |
| ERL | 150 | 36 | 2.3 |

decreasing the sampling ratio reduces the stability of the HIO algorithm convergence to a valid solution, though resolution is improved for a smaller sampling ratio (larger detector pixel size), if only successful reconstructions are taken for averaging. The addition of more constraints to the phasing algorithm owing to *a priori* information may be possible, such as the widely used histogram constraint. This may allow reduced oversampling.

Note that all calculations have been carried out for one sample in the beam. Application of a ‘shower head’ multiplex-nozzle aerogel array, which is currently under development, has the potential to increase the number of molecules simultaneously present in the beam to about 100. This would substantially reduce the time required for diffraction measurement.

In summary, when full account is taken of Poisson noise and the performance of the phasing algorithm, we find using equation (10) that the exposure time for serial crystallography is given by

$$\Delta t = \frac{1.3 \times 10^9 s^2}{M I_0 d^4 \lambda^2}, \quad (19)$$

where we use units of nm and s, and the scaling constant is derived from Fig. 7. The severe dependence on the poorly defined resolution d is noted. (d is poorly defined because it depends on the structure of the sample. Our resolution definition using $\text{MTF} = 0.5$ is highly conservative.) This power law has serious implications for all attempts at coherent imaging with X-rays. Table 1 shows estimates of the expected counting times at the planned ALS, APS and ERL X-ray beamlines from equation (19), which demonstrate a severe punishment in terms of the required exposure time for a very small resolution improvement. We note that, under the dose fractionation theorem of Hegerl & Hoppe (1976), these times are increased by a factor of 40 for three-dimensional image data collection.

5. Summary

The simple way to estimate the diffraction experiment counting time required for a given resolution is to calculate the number of photons scattered at the angle corresponding to this resolution and to set this number to a fixed value, which would provide the statistically accurate measurement. We performed this calculation analytically for a globular uniform object and numerically by simulating the diffraction pattern for the chaperonin GroEL–GroES protein complex. This approach gives the lower limit of the required exposure. For a

more elaborate evaluation, which also accounts for the convergence stability of the phase-retrieval algorithm and its effect on resolution, we have used the HIO procedure to reconstruct charge density maps in real space from simulated diffraction patterns with different noise levels. Visual examination of the reconstructed images shows that at the projected ERL X-ray beam source even a short exposure of 10–100 s can produce valuable information on the bio-complex envelope shape. Using the transfer function spatial frequency cut-off as a quantitative measure of resolution, we determined the functional dependence of the exposure time on required resolution. It scales as the inverse fourth power of d . Using the count rate, required for a statistically accurate measurement, as a free parameter, we obtain an exact agreement with the analytical solution. However, the prefactor obtained by fitting to the calculated resolution is higher than that expected from the Rose criterion.

The times predicted by the simple analytical models given here and by Henke & DuMond (1955), Howells *et al.* (2005) and Shen *et al.* (2004) can be up to two orders of magnitude shorter than those following from the TF calculation, since they do not include the effects of the phasing algorithm on resolution. These three analytical model treatments may be distinguished as follows.

(i) In Henke & DuMond (1955) and Howells *et al.* (2005), a coherent sum of scattering from one voxel (resolution element) inside the sample is used. The result depends on which voxel is chosen.

(ii) In Shen *et al.* (2004), an incoherent sum over all voxels is used at the maximum (resolution limiting) scattering angle. Interference between waves scattered by different voxels is eliminated by averaging, and the result depends on molecular size. We note a d^{-3} scaling of exposure time in this approach.

(iii) In our treatment, a coherent shape scattering at the maximum (resolution limiting) scattering angle is used. The result again depends on the size of the molecule.

The reported results have important implications for the design of droplet beam systems for serial crystallography, suggesting that the use of multiple nozzles will be essential for third-generation synchrotrons but not for fourth-generation machines.

Possibilities for decreasing the exposure time required to achieve a desired resolution include use of lower X-ray energy, optimization of coherence conditions, increasing the number M of proteins present in the X-ray beam at any instant, use of a more efficient phasing algorithm (Marchesini, 2007) and use of additional constraints, such as the histogram constraint (which drives the density map towards the known gray-level histogram for protein density maps), allowing a smaller sampling ratio s . Additional *a priori* information may also be available, such as bond lengths and sequence. The method of molecular replacement may also be useful, and has now succeeded in solving a protein structure from powder diffraction data (Von Dreele *et al.*, 2000). Taken together, these improvements would reduce the required exposure at the ERL down to a value of a few tens of seconds.

This work was supported by ARO grant DAAD190010500 and NSF award IDBR 0555845.

References

- Bras, W., Diakun, G. P., Díaz, J. F., Maret, G., Kramer, H., Bordas, J. & Medrano, F. J. (1998). *Biophys. J.* **74**, 1509–1521.
- Chapman, H. N., Barty, A., Marchesini, S., Noy, A., Hau-Riege, S. P., Cui, C., Howells, M. R., Rosen, R., He, H., Spence, J. C. H., Weierstall, U., Beetz, T., Jacobsen, C. & Shapiro, D. A. (2006b). *J. Opt. Soc. Am. A*, **23**, 1179–1200.
- Chapman, H. N. *et al.* (2006a). *Nat. Phys.* **2**, 839–843.
- Chaudhry, C., Horwich, A. L., Brunger, A. T. & Adams, P. D. (2004). *J. Mol. Biol.* **342**, 229–245.
- Doyle, P. A. & Turner, P. S. (1968). *Acta Cryst.* **A24**, 390–397.
- Fienup, J. R. (1982). *Appl. Opt.* **21**, 2758–2769.
- Fienup, J. R. (1997). *Appl. Opt.* **36**, 8352–8357.
- Fredericq, E. & Houssier, C. (1973). *Electric Dichroism and Electric Birefringence*. Oxford: Clarendon Press.
- Hegerl, R. & Hoppe, W. (1976). *Z. Naturforsch. A*, **31**, 1717–1721.
- Henderson, R. (1995). *Q. Rev. Biophys.* **28**, 171–193.
- Henke, B. L. & DuMond, J. W. M. (1955). *J. Appl. Phys.* **26**, 903–917.
- Henke, B. L., Gullikson, E. M. & Davis, J. C. (1993). *Atom. Data Nucl. Data Tables*, **54**, 181–342.
- Howells, M. R., Beetz, T., Chapman, H. N., Cui, C., Holton, J. M., Jacobsen, C. J., Kirz, J., Lima, E., Marchesini, S., Miao, H., Sayre, D., Shapiro, D. A. & Spence, J. C. H. (2005). arxiv.org e-print archive, <http://arxiv.org/pdf/physics/0502059>.
- Huldt, G., Szoke, A. & Hajdu, J. (2003). *J. Struct. Biol.* **144**, 219–227.
- Koch, M. H. J., Dorrington, E., Klaring, R., Michon, A. M., Sayers, Z., Marquet, R. & Houssier, C. (1988). *Science*, **240**, 194–196.
- McEwen, B. F., Downing, K. H. & Glaeser, R. M. (1995). *Ultramicroscopy*, **60**, 357–373.
- Marchesini, S. (2007). *Rev. Sci. Instrum.* **78**, 011301.
- Marchesini, S., Chapman, H. N., Barty, A., Howells, M. R., Spence, J. C. H., Cui, C., Weierstall, U. & Minor, A. M. (2005). *Proceedings of the 8th International Conference on X-ray Microscopy*, pp. 380–382, Himeji, Japan.
- Marchesini, S., Chapman, H. N., Hau-Riege, S. P., London, R., Szoke, A., He, H., Howells, M., Padmore, H., Rosen, R., Spence, J. C. H. & Weierstall, U. (2003). *Opt. Express*, **11**, 2344–2353.
- Marchesini, S., He, H., Chapman, H. N., Hau-Riege, S. P., Noy, A., Howells, M. R., Weierstall, U. & Spence, J. C. H. (2003). *Phys. Rev. B*, **68**, 140101(R).
- Rayleigh, J. S. W. (1878). *Proc. London Math. Soc.* **10**, 4–13.
- Rose, A. (1948). *Advances in Electronics and Electron Physics*, edited by L. Marton, Vol. 1, pp. 131–166. New York: Academic Press.
- Shapiro, D., Thibault, P., Beetz, T., Elser, V., Howells, M., Jacobsen, C., Kirz, J., Lima, E., Miao, H., Neiman, A. M. & Sayre, D. (2005). *Proc. Natl. Acad. Sci. USA*, **102**, 15343–15346.
- Shen, Q., Bazarov, I. & Thibault, P. (2004). *J. Synchrotron Rad.* **11**, 432–438.
- Sobott, F., McCammon, M. G., Hernandez, H. & Robinson, C. V. (2005). *Philos. Trans. R. Soc. London A*, **363**, 379–389.
- Spence, J. C. H. & Doak, R. B. (2004). *Phys. Rev. Lett.* **92**, 198102.
- Spence, J. C. H. & Howells, M. R. (2002). *Ultramicroscopy*, **93**, 213–222.
- Spence, J. C. H., Schmidt, K., Wu, J. S., Hembree, G., Weierstall, U., Doak, R. B. & Fromme, P. (2005). *Acta Cryst.* **A61**, 237–245.
- Spence, J. C. H., Weierstall, U. & Howells, M. (2004). *Ultramicroscopy*, **101**, 149–152.
- Starodub, D., Doak, R. B., Schmidt, K., Weierstall, U., Wu, J. S., Spence, J. C. H., Howells, M., Marcus, M., Shapiro, D. A., Barty, A. & Chapman, H. N. (2005). *J. Chem. Phys.* **123**, 244304.

- Von Dreele, R. B., Stephens, P. W., Smith, G. D. & Blessing, R. H. (2000). *Acta Cryst. D* **56**, 1549–1553.
- Weierstall, U., Doak, R. B., Spence, J. C. H., Starodub, D., Shapiro, D. A., Kennedy, P., Warner, J., Hembree, G. G., Fromme, P. & Chapman, H. N. (2007). arxiv.org e-print archive, <http://arxiv.org/abs/physics/0701129>.
- Wu, J. S., Leinenweber, K., Spence, J. C. H. & O’Keeffe, M. (2006). *Nat. Mater.* **5**, 647–652.
- Young, L., Arms, D. A., Dufresne, E. M., Dunford, R. W., Ederer, D. L., Höhr, C., Kanter, E. P., Krässig, B., Landahl, E. C., Peterson, E. R., Rudati, J., Santra, R. & Southworth, S. H. (2006). *Phys. Rev. Lett.* **97**, 083601.